Advanced Steel Construction – Vol. 20 No. 3 (2024) 310–318
DOI:10.18057/IJASC.2024.20.3.10

A MODEL FOR PREDICTING THE MOMENT-CURVATURE BEHAVIOR OF STEEL TUBE CONFINED REINFORCED SELF-STRESSING STEEL SLAG CONCRETE COLUMNS UNDER CYCLIC LOADING

Feng Yu [1, 2], Wei Liu [1], Shuang-Shuang Bu [1, *], Guang-Fei Kuang [1] and Yuan Fang [1]

[1] *Department of Civil Engineering and Architecture, Anhui University of Technology, Maanshan, 243032, China*
[2] *Wuhu Technology and Innovation Research Institute, Anhui University of Technology, Wuhu, 241002, China*
** (Corresponding author: E-mail: biluo12345@163.com)*

ABSTRACT

This paper evaluates the moment-curvature response of steel tube confined reinforced self-stressing steel slag concrete (STCRSSSC) columns by conducting cyclic loading tests on ten STCRSSSC columns and four steel tube confined reinforced steel slag concrete (STCRSSC) columns. Four parameters are considered: axial compression ratio, shear-span ratio, diameter-thickness ratio, and expansion rate of steel slag concrete (SSC). The results show that the specimens exhibit a bending failure mode. As the expansion rate of SSC or shear-span ratio increase, the area of the moment-curvature $M-\phi$ hysteretic loops expands, but the slope of the skeleton curve remains basically unchanged. The slope of the skeleton curve rises as the diameter-thickness ratio or axial compression ratio increase. With the reduction of the axial compression ratio or diameter-thickness ratio, the area of the $M-\phi$ hysteretic loops increases. Based on the experimental results, the characteristic points of the $M-\phi$ response are identified, and a simplified model is proposed to predict the skeleton curves. Lastly, a hysteresis rule of the specimens is suggested based on the Clough trilinear degeneration model, and a predicting model of the $M-\phi$ response of the specimens is established.

ARTICLE HISTORY

Received: 13 October 2023
Revised: 8 April 2024
Accepted: 21 April 2024

KEYWORDS

Concrete-filled steel tube;
Steel tube confined concrete;
Steel slag;
Self-stressing concrete;
Hysteresis behavior;
Restoring force model

1. Introduction

Steel tube confined concrete (STCC) columns are widely used in engineering owing to their significant advantages such as excellent ductility, high bearing capacity, and convenient construction [1-5]. However, shrinkage of the concrete core leads to a reduction in the bonding performance between the steel tube and concrete core, which can significantly weaken the bearing capacity and safety of the structures [6-7].

To solve the shrinkage problem of the core concrete, self-stressing concrete is used as an effective solution to balance the shrinkage of the core concrete and promote collaboration between the steel tube and core concrete [8-9]. Traditional self-stressing concrete is produced by adding expansion agents, and it has been proven that the bond behavior of self-stressing concrete-filled steel tubes (SCFST) can be improved by increasing the content of the expansive agent [10-12]. Subsequently, some scholars carried out a series of further studies and revealed that SCFST columns exhibit excellent axial compressive behaviors, flexural capacity, and seismic properties [13-17]. However, the extensive use of expansion agents in practical engineering applications has resulted in problems such as high construction costs and preparation complexity.

Steel slag concrete (SSC) is prepared using steel slag as an aggregate, and appropriate proportions can guarantee the mechanical properties and durability of SSC [18-22]. It has been proven to have potential for engineering applications [23-24]. In addition, the volumetric expansion of SCC after hydration is caused by the presence of free CaO/MgO in the steel slag. This characteristic makes it possible to satisfy the expansion performance requirements of self-stressing concrete [25]. Self-stressing steel slag concrete can not only solve the problems of high cost and complex preparation of traditional self-stressing concrete but also improve the mass utilization of steel slag.

Combining the advantages of SCFST and the expansion performance of SSC, Yu et al. investigated the feasibility of preparing self-stressing SSC-filled steel tubular (SSSCFST) columns. It appears that increasing the expansion rate of the SSSC may lead to an improvement in both the compression performance and bond-slip behaviors of the specimens [26-28]. However, current studies on the behavior of steel tube confined reinforced self-stressing SSC (STCRSSSC) under different loading conditions are limited.

Seismic performance is crucial for structural applications and designs. In this study, four steel tube confined reinforced steel slag concrete (STCRSSC) columns and ten STCRSSSC columns were used. Furthermore, this study analyzed and discussed the effects of the diameter-thickness ratio, axial compression ratio, expansion rate of SSC, and shear-span ratio on the seismic behaviors of the specimens. Finally, an analysis model for evaluating the $M-\phi$ behavior of STCRSSSC columns is established, which is expected to complete the elastoplastic seismic response analysis of such composite structures.

2. Experimental program

2.1. Specimens design

Ten STCRSSSC columns and four STCRSSC columns are presented in this paper. As shown in Fig. 1, the entire specimen was designed to have an inverted T-shape. The specimen consisted of a column head, column body, and foundation. The total height of the specimen was 1600 mm. The height of the column head was 400 mm. The heights of the column bodies were 400, 600, and 800 mm. The shear-span ratio, axial compression ratio, diameter-thickness ratio, and expansion rate of SSC are listed in Table 1.

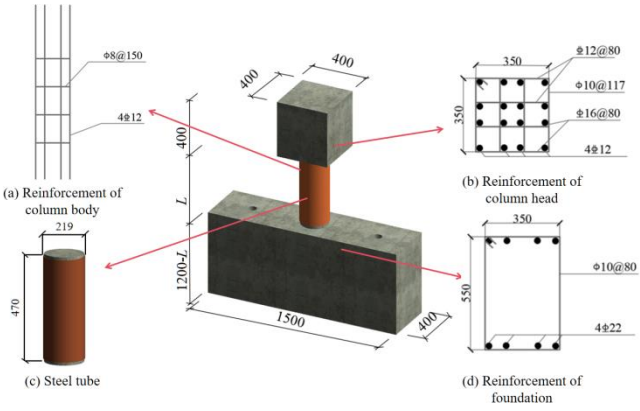

Fig. 1 Details of the specimens

As shown in Fig. 1(c), the outer diameter and height of the steel tube were 219 and 470 mm, respectively. To ensure the restraining effect of the steel tube on the concrete core, the ends of the steel tube were spaced 15 mm apart from the foundation and column head. The thicknesses of the steel tubes were 2.85, 3.73, and 4.88 mm, respectively. Longitudinal steel bars of the column body were 4C12 with a longitudinal bar ratio of 1.210%, whereas the stirrups were A8@150 with a stirrup ratio of 0.022%. Table 1 lists the specific design parameters.

2.2. Material properties

2.2.1. SSC

According to references [29-32], the axial and cube compressive strength of the SSSC are 26.33 MPa and 39.30 MPa, respectively, while the axial and cube compressive strength of the SSC are 24.41 MPa and 36.44 MPa, respectively. To determine the expansion rate of the SSC P_{ct}, three test blocks were constructed and tested, as shown in Fig. 2, and the value of P_{ct} was obtained using Eq. (1).

$$P_{ct} = \frac{L_t - L_e}{L_0} \tag{1}$$

where L_t is the distance between the two copper heads measured over 90 days, L_0 is the initial distance between the two copper heads, and $L_e = 250$ mm is the reference distance.

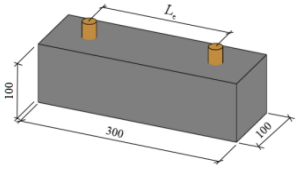

Fig. 2 Test specimen used to determine the expansion rate of SSC

2.2.2. Steel tube

Longitudinal and circumferential strains were measured using strain gauges according to the Chinese code [32]. The material properties are listed in Table 2.

Table 1
Specimen design parameters

Specimen label	L (mm)	D (mm)	t (mm)	n_0	D/t	λ	P_{ct} ($\times 10^{-4}$)
A1	800	219	2.85	0.2	76.8	1.83	11.1
A2	800	219	3.73	0.2	58.7	1.83	11.1
A3	800	219	4.88	0.2	44.8	1.83	11.1
A4	600	219	2.85	0.2	76.8	1.37	11.1
A5	400	219	2.85	0.2	76.8	0.91	11.1
A6	800	219	2.85	0.4	76.8	1.83	11.1
A7	800	219	3.73	0.4	58.7	1.83	11.1
A8	800	219	4.88	0.4	44.8	1.83	11.1
A9	600	219	2.85	0.4	76.8	1.37	11.1
A10	400	219	2.85	0.4	76.8	0.91	11.1
B1	800	219	2.85	0.2	76.8	1.83	-3.5
B2	600	219	2.85	0.2	76.8	1.37	-3.5
B3	400	219	2.85	0.2	76.8	0.91	-3.5
B4	800	219	2.85	0.4	76.8	1.83	-3.5

Note: L is the length of the column, t is the thickness of the steel tube, D is the outer diameter of the steel tube, D/t is the diameter-thickness ratio, n_0 is the axial compression ratio, $n_0 = N_a / f_c A_c$, N_a is the designed axial compression strength of the specimen, A_c is the cross-sectional area of the column, f_c is the compressive strength of the SSC, and λ is the shear-span ratio, $\lambda = L/2D$.

Table 2
Mechanical properties of the steel tube

Thickness (mm)	Yield tensile strength (MPa)	Ultimate tensile strength (MPa)	Young's modulus ($\times 10^5$ MPa)	Poisson's ratio	Longitudinal strain ($\times 10^{-6}$ mm)	Circumferential strain ($\times 10^{-6}$ mm)	Initial self-stress (MPa)
2.85	308	479	2.00	0.313	3.92	1.93	2.68
3.73	364	495	2.11	0.271	3.33	1.65	3.03
4.88	335	480	2.06	0.261	2.79	1.41	3.26

2.2.3. Steel bars

The tensile samples of the steel bars were tested according to the Chinese code [33] and were listed in Table 3.

Table 3
Mechanical properties of the steel bars

Steel bars	Diameter (mm)	Yield strength (MPa)	Tensile strength (MPa)	Young's modulus ($\times 10^5$ MPa)
HPB300	8	308	426	2.01
HPB300	10	313	432	1.97
HRB400	12	439	644	1.98
HRB400	16	451	620	1.95
HRB400	22	438	618	1.94

2.3. Loading protocol and test setup

Fig. 3 shows a diagram of the loading device. A constant axial load and cyclic lateral loading were applied using a vertical jack and an MTS hydraulic

actuator, respectively. In this experiment, a displacement-loading control method was adopted. First, ensure that the test equipment works properly and that the axial load is applied slowly to the design value. Before the specimen yielded, a single-cycle displacement with increments of 1 mm was used for horizontal loading. After the specimen yielded, the loading mode was switched to a triple-cycle displacement with increments in integral multiples of the yield displacement. A specimen was considered damaged when its strength decreased to 85% of its peak load.

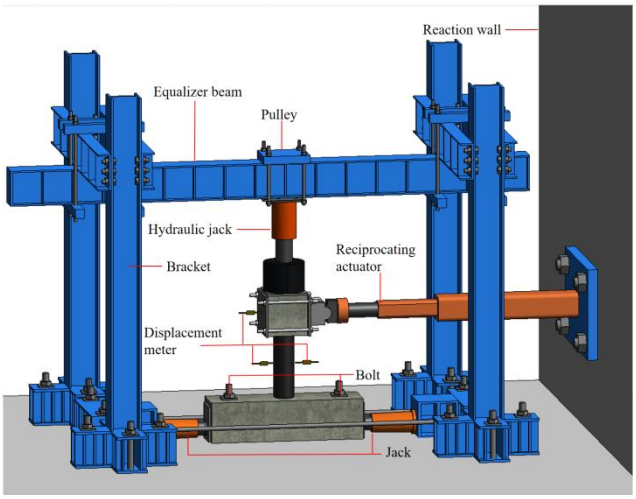

Fig. 3 Test setup: (a) reaction wall, (b) pulley, (c) hydraulic jack, (d) reciprocating actuator, (e) counter-force truss, (f) specimen, (g) jack, (h) bracket, (i) equalizer beam, (j) portal frame, (k) loading plate, (l) displacement meter, (m) bolt

3. Experimental results

3.1. Failure mode

Bending failure was observed as the typical failure mode of the STCRSSSC and STCRSSC columns, represented by the crushing of the SSC, yielding of the steel tubes and stirrups and circumferential tensile cracks in the inner core SSC. As illustrated in Fig. 4(a), the core SSC was crushed to a height of 0-15 mm, and circumferential tensile cracks appeared within a height of 15--60 mm from the bottom of the column. No damage was observed at other positions on the STCRSSSC columns. However, for the STCRSSC columns, as shown in Fig. 4(b), the degree of SSC crushing was more severe, and the range of heights in which circumferential tension cracks. Compared to the literature [34], the failure modes of the specimens were almost identical.

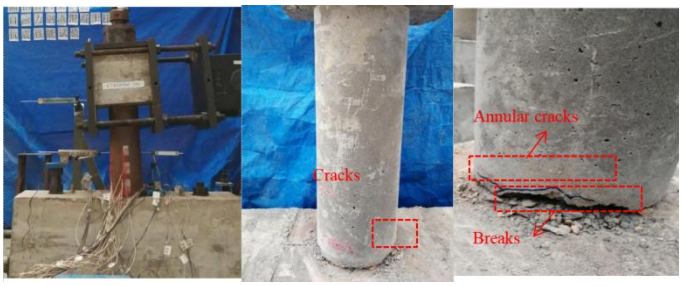

(a) A9 of the STCRSSSC column

(b) B4 of the STCRSSC column

Fig. 4 Typical failure mode of the specimens

3.2. Hysteresis curve

As shown in Fig. 5, the hysteresis loops of the specimens are saturated and slightly pinched. The $M-\phi$ hysteresis curves usually have three stages: elastic response, yielding and failure. The $M-\phi$ hysteresis curves appear to develop linearly in the elastic stage, with stiffness degradation remaining basically unchanged, and the hysteretic loops being very small. The hysteresis curves gradually deviate from the initial linear development as the load gradually increases. As the specimen enters the yield stage, the hysteresis loop area increases compared with the elastic stage. In the failure stage, the bow-shaped hysteretic loop with a slight pinching phenomenon indicates that the specimen exhibited high seismic performance and energy dissipation.

As shown in Figs. 5(a) and (f), an increase in the axial compression ratio decreases the plumpness of the $M-\phi$ hysteresis curves and the area of the hysteretic loops. For example, compared to specimen A1 ($n_0=0.2$), the ultimate moment of specimen A6 ($n_0=0.4$) increased by 17.30%. The reason for this might be that, with the increase in n_0 , the axial force at the end of the column increases. The tensile stress generated by the axial force resisting the bending moment was enhanced, leading the specimen to resist a higher bending moment. The ultimate curvature of the $M-\phi$ hysteresis curves decreases when n_0 increases, because higher axial forces lead to an increase in additional bending moments, accelerating specimen damage. The same effect of n_0 on the $M-\phi$ hysteresis curves of reinforced SCC-filled circular steel-tube columns was found by Gong et al. [35].

As shown in Figs. 5(a) and (d), the growth rate of the bending moment remains essentially unchanged as λ increases, whereas that of the $M-\phi$ hysteresis curves decreases and the area of the hysteresis loops increases. This is because as the shear-span ratio increases, the specimen's cross-sectional deformability increases, resulting in an increase in the specimen's cross-sectional curvature. This conclusion was also verified by Yu et al. [36], who demonstrated that the ductility capacity increased with an increase in λ .

In general, as illustrated in Figs. 5(a) and (b), an increase in D/t accelerates the growth rate of the bending moment, reduces the area of the hysteretic loops, and intensifies the pinching phenomenon. Furthermore, the bending moment of the specimen section decreased, the curvature increased and the cycle number of the $M-\phi$ hysteresis curves decreased before the specimens failed. The cross-sectional moment of inertia of the core SSSC increased as D/t increased, whereas that of the steel tube decreased. Consequently, the overall bending stiffness of the specimens improved, but the ductility decreased. The increase in D/t produces the same effect on the CFST [37].

As shown in Figs. 5(d) and (l), the increment in P_{ct} results in an improvement in the bending moment growth rate, an increase in the hysteretic loop area, and a reduction in the pinching degree. This may be because increasing P_{ct} improves the expansion strain of the SSC under the constraint of the steel tube, leading to a dense specimen structure and reduced porosity. Therefore, the deformation resistance and bearing capacity of the specimens were enhanced. A similar conclusion was drawn by Dai et al. [38]. Meanwhile, the bond-slip between the steel tube and core SSSC decreased, and the pinching phenomenon of the $M-\phi$ hysteresis curves was significantly reduced. It is difficult to control the P_{ct} and performance of STCRSSSC in practical engineering designs and applications, which requires further research.

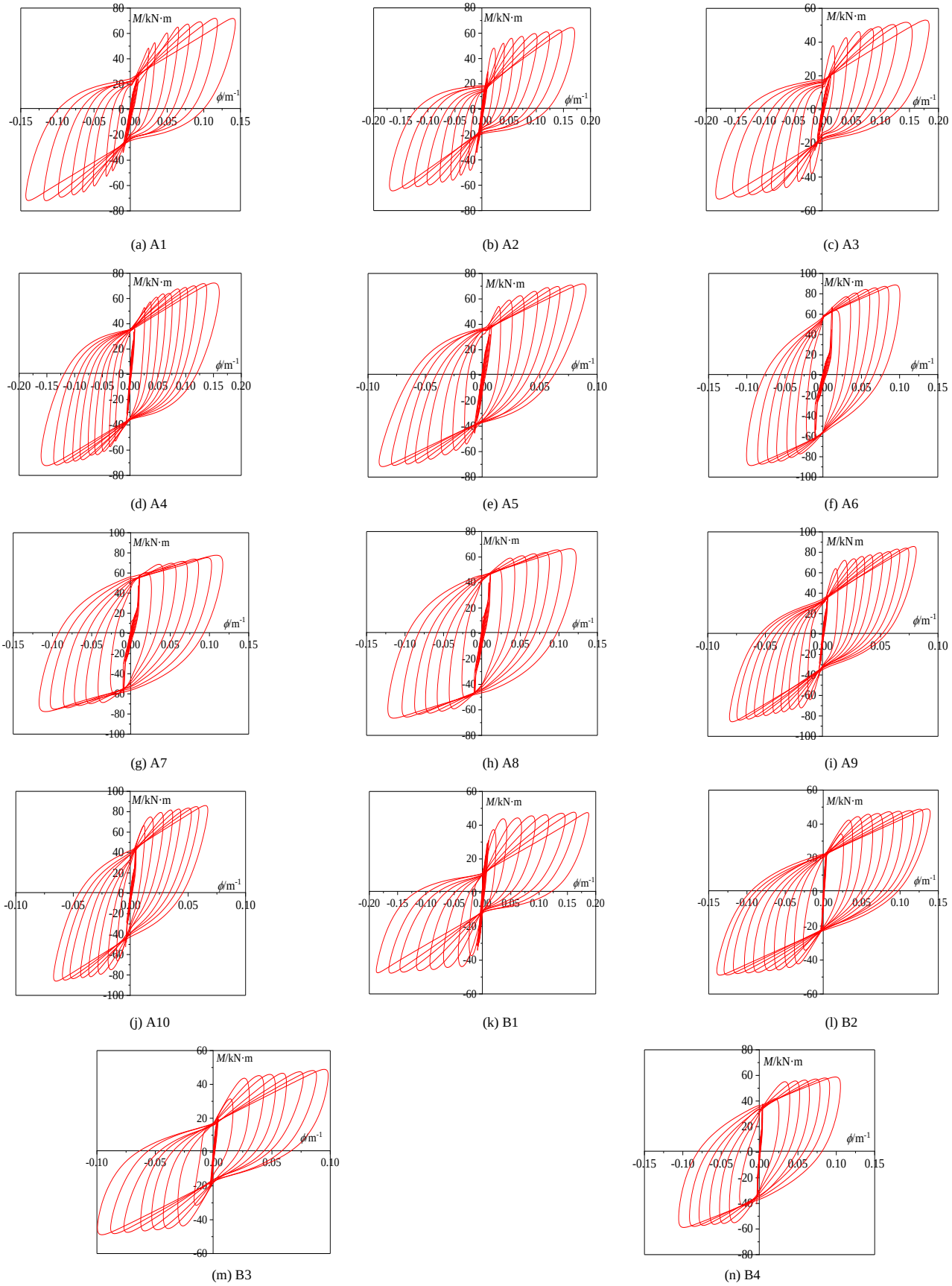

(a) A1 (b) A2 (c) A3

(d) A4 (e) A5 (f) A6

(g) A7 (h) A8 (i) A9

(j) A10 (k) B1 (l) B2

(m) B3 (n) B4

Fig. 5 Moment-curvature hysteresis curves

3.3. Skeleton curve

The $M-\phi$ skeleton curve can be approximately divided into three stages, similar to the hysteresis curve shown in Fig. 6. The $M-\phi$ skeleton curves appeared linear in the elastic phase. Subsequently, with an increase in the horizontal displacement, the $M-\phi$ skeleton curves gradually exhibited nonlinear development, and an inflection point appeared. The slopes of the $M-\phi$ skeleton curves decreased, and the cross-sectional bending stiffness gradually degraded in the yield phase, intensifying during the failure stage.

As shown in Fig. 6(a), as n_0 increased, the peak moment, initial stiffness, and slope of the $M-\phi$ skeleton curves increased, whereas the ultimate curvature decreased. In contrast to specimen A5 ($n_0=0.2$), the ultimate moment of specimen A10 ($n_0=0.4$) increases by 20.25%. Additionally, as the axial compression ratio decreased, the ultimate curvature increased. This could be because the core SSSC of the specimen was destroyed when the peak load was reached, reducing the bending stiffness of the specimens. The degradation of bending stiffness is significantly accelerated if severe damage is caused to the SSSC core. The seismic behavior of STCRSSSC columns is more significantly affected by n_0 , so further research should be carried out to propose a more appropriate design value for n_0 to ensure the safety of structures in practical engineering applications.

Fig. 6(b) illustrates that the $M-\phi$ skeleton curve was not significantly affected by λ . As λ increased, the slopes of the $M-\phi$ skeleton curves and the ultimate bending moment hardly changed. It can be argued that the cross-sectional bending stiffness is primarily influenced by the cross-sectional moment of inertia and the Young's modulus of the specimen. The influence of the λ on the bending stiffness was not significant when the height of the specimens was adjusted.

As D/t increases, the slopes of the $M-\phi$ skeleton curves, peak moment, and initial stiffness increase, whereas the peak curvature decreases, as shown in Fig. 6(c). The ultimate moment of the specimens increased, and the ultimate curvature decreased with increasing D/t . Considering specimens A1 and A3 as examples, when D/t was reduced by 41.67%, the ultimate curvature of A3 was 1.29 times that of A1. This was because the bending stiffness of the specimens increased, leading to an increase in the load when the specimen was damaged. The SSSC was significantly damaged, resulting in a decrease in the bearing capacity of the specimens. The limited value of D/t of STCRSSSC columns must be further explored to ensure the adequate seismic performance and economy of the columns.

Fig. 6(d) shows that the slope of the $M-\phi$ skeleton curves increases slightly, the initial stiffness and yield bending capacity increase, and the ultimate moment and curvature increase with the increment in P_{ct} . For example, the ultimate moment of A4 ($P_{ct}=11.1\times10^{-4}$) is 1.50 times that of B2 ($P_{ct}=-3.5\times10^{-4}$), and the ultimate curvature is 1.12 times. This may be because the increasing expansion rate of the SSC enhances the confining effect on the SSSC, decreases the damage degree of the SSSC, and improves the bending capacity and ductility of the specimens. The increased ductility of the specimen was mainly due to the expansion of SSC, even when the steel tube was replaced with an FRP tube [39].

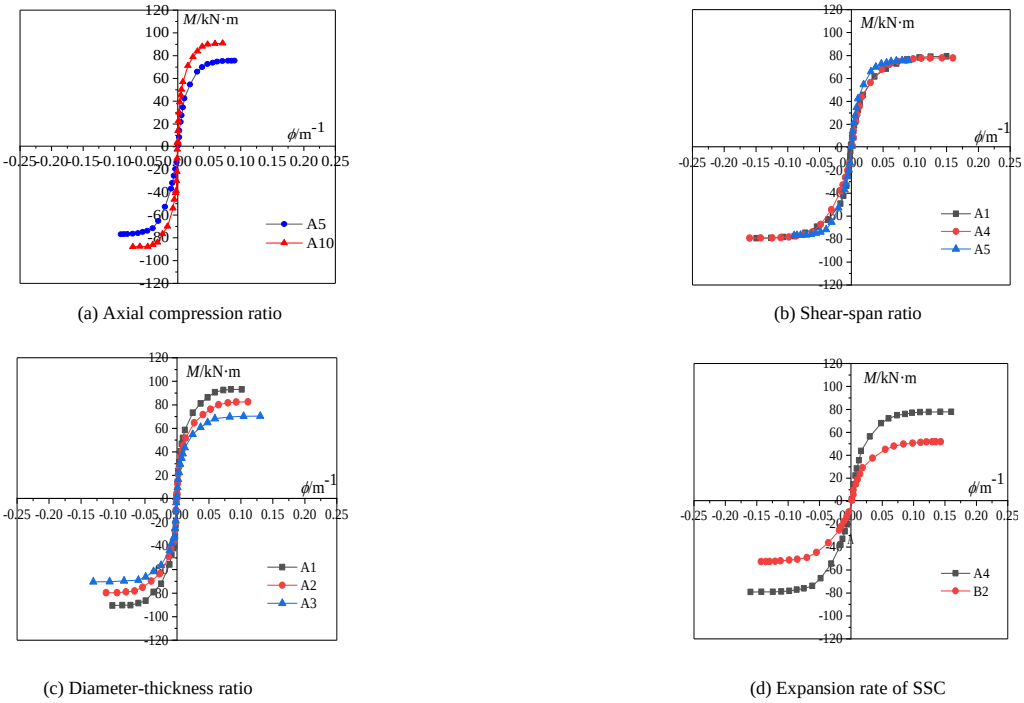

(a) Axial compression ratio

(b) Shear-span ratio

(c) Diameter-thickness ratio

(d) Expansion rate of SSC

Fig. 6 Effects of the studied parameters on the skeleton curves of the specimens

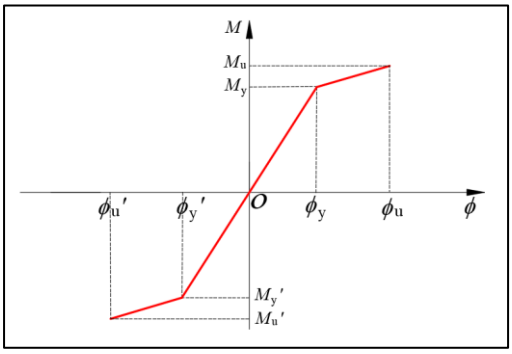

Fig. 7 Simplified STCRSSSC columns moment-curvature skeleton curve

4. Model for predicting the moment-curvature performance of STCRSSSC columns

4.1. Prediction of the moment-curvature skeleton curves

Based on the limiting equilibrium principle, a simplified calculation model for predicting $M-\phi$ skeleton curves was proposed. Subsequently, four key parameters yield moment (M_y), ultimate moment (M_u), yield curvature (ϕ_y), and ultimate curvature (ϕ_u) of the $M-\phi$ skeleton curves were determined. The simplified $M-\phi$ skeleton curves were determined by connecting the four key parameters, as indicated in Fig. 7.

4.1.1. Basic assumptions

To establish a prediction model for the moment-curvature performance of STCRSSSC columns, the following assumptions were made:

(1) The specimen's cross-section remained plane.

(2) There was no relative slip between the steel bars, SSC, and steel tube.

(3) The effect of core SSSC in the tension zone was not considered.

(4) The longitudinal stress in the steel tube owing to the tensile expansion of the SSSC was not considered.

(5) The axial force applied to the section was constant.

(6) The constitutive model described in [40] was assigned to the core SSSC.

4.1.2. Yield moment and curvature

According to reference [40], the yield moment M_y can be obtained using Eqs. (2).

$$M_y = 1.59 f_{ccy}^e r_c^3 + 0.0037 N \sigma_z r_c - 19 r_c^3 + 0.57 f_{sy} \rho_s A_{sc} r_c \tag{2}$$

where f_{ccy}^e denotes the stress of the core SSSC in the compression zone of the critical section, r_c denotes the radius of the core SSSC section, N denotes the axial compression of the SSSC core, σ_z indicates the longitudinal self-stress caused by the initial self-stress, ρ_s represents the steel ratio of the steel ring, A_{sc} refers to the cross-sectional area of the column, and f_{sy} represents the yield strength of the longitudinal reinforcement.

The yield curvature can be obtained from Eq. (3).

$$\phi_y = \frac{M_y}{K_{sc}} \tag{3}$$

where ϕ_y is the yield curvature of the specimen, K_{sc} is the sectional bending stiffness of the STCRSSSC column, $K_{sc} = E_{sc} I_c$, E_{sc} denotes the section deformation modulus of the STCRSSSC column, $E_{sc} = f_{ccy}^e / \varepsilon_{y1}$, ε_{y1} designates the longitudinal strain of the specimen, and I_c is the sectional inertia moment of the STCRSSSC column, $I_c = \pi (D - 2r_c)^4 / 64$.

4.1.3. Ultimate moment and curvature

According to [40], the ultimate moment M_u considering the effects of the axial force, low-cycle reversed loading, and initial self-stress of the core SSSC on the bending capacity can be expressed as Eq. (4).

$$M_u = 1.59 f_{cc}^e r_c^3 - 19 r_c^3 + 0.037 N \sigma_z r_c + 0.95 f_{ss} \rho_s A_{sc} r_c \tag{4}$$

where f_{cc}^e is the strength of the confined core SSSC and f_{ss} denotes the actual strength of the longitudinal reinforcement.

The average strain along the height of the cross-section was linear based on the plane section assumption. Therefore, the ultimate curvature ϕ_u is calculated as follows:

$$\phi_u = \frac{\varepsilon_{cu}}{\zeta} = \frac{\varepsilon_{sy}(r_c \cos\gamma_0 + r_c - m) E_s + m f_{ss}}{m r_g E_s} \tag{5}$$

$$\varepsilon_{cu} = \frac{\varepsilon_{sy}(r_c \cos\gamma_0 + r_c - m)}{m} \tag{6}$$

$$\zeta = \frac{r_g \varepsilon_{cu}}{\varepsilon_{cu} + \varepsilon_{sy}} = \frac{r_g E_s \varepsilon_{cu}}{f_{sy} + E_s \varepsilon_{cu}} \tag{7}$$

$$m = \frac{(2r_c - a)\varepsilon_{sy}}{\varepsilon_{sy} + \varepsilon_{cu}} \tag{8}$$

$$\gamma_0 = \frac{\pi}{2} - \arccos\frac{2m - r_g}{r_g} \tag{9}$$

$$r_g = r_c - a \tag{10}$$

where ε_{cu} is the ultimate strain of the confined core SSSC, ε_{sy} is the yield compression strain of the steel ring, E_S is the Young's modulus of the steel tube, m stands for the distance from ε_{sy} to strain 0, ζ designates the height of the core SSSC in the compression zone, γ_0 indicates the center angle of the core SSSC in the compression zone, r_g is the radius of the equivalent steel ring of longitudinal reinforcement, and a is the radius of the core SSSC section in the tensile zone.

4.1.4. Assessment of the proposed skeleton curve prediction model

Fig. 8 compares the proposed $M-\phi$ and experimental $M-\phi$ skeleton curves. The experimental results were in good agreement with the theoretical curves, demonstrating the high accuracy of the proposed model.

4.2. Hysteresis rule

Based on the numerical analysis of the $M-\phi$ skeleton curves for each factor, a Cough trilinear degeneration model was adopted to further analyze the $M-\phi$ hysteresis rules of the STCRSSSC columns. The parameters were determined using Eqs. (11)–(17), as shown in Fig. 9.

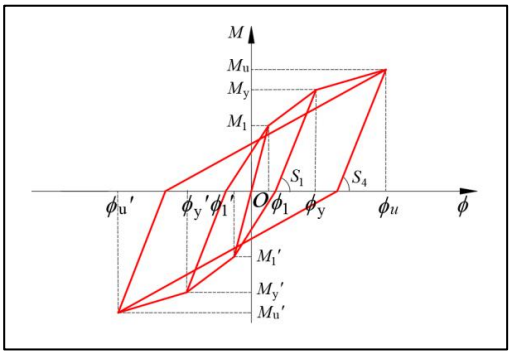

Fig. 9 Loading and unloading rules for STCRSSSC columns under cyclic loading

$$S_1 = \frac{M_1}{\phi_1} \tag{11}$$

$$S_2 = \frac{M_y}{\phi_y} \tag{12}$$

$$M_1 = 0.6 M_y \tag{13}$$

$$S_3 = 0.112 n_0 + 2.864 \sigma_0 + 0.003 D/t - 1.443 \lambda + 0.883 \tag{14}$$

$$S_4 = S_1 \tag{15}$$

$$S_5 = S_1 \left(\frac{\phi_i}{\phi_y}\right)^{\beta} \tag{16}$$

$$\beta = 0.140 n_0 - 0.019 \lambda - 0.003 D/t + 0.133 \sigma_0 + 0.265 \tag{17}$$

where S_1 and S_2 denote the stiffnesses at the elastic and yield stages, respectively, M_1 and ϕ_1 denote the bending moment and curvature, respectively, S_3 indicates the stiffness in the third stage, M_u represents the ultimate moment, S_4 and S_5 are the unloading stiffnesses before and after yielding, respectively, ϕ_i is the curvature corresponding to the i-th unloading point of the $M-\phi$ curve starting from the yield point, and β is an parameter related to D/t, λ, n_0, and the initial self-stress.

4.3. Verification of the model for predicting the moment-curvature response of the specimens

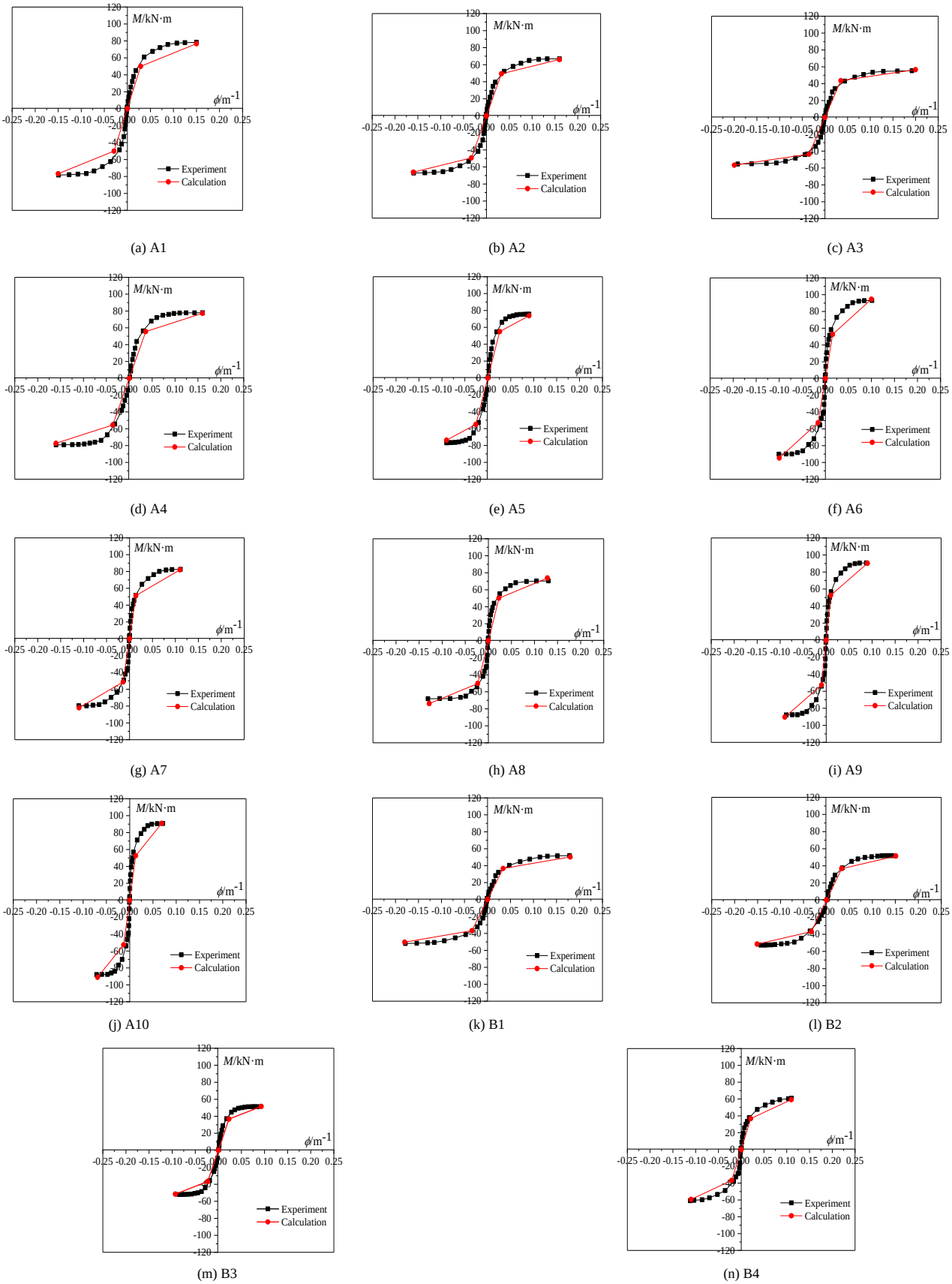

Fig. 8 Verification of experimental and theoretical moment-curvature skeleton curves

The predicted hysteresis curves can be obtained by calculating the skeleton curves of the $M-\phi$ hysteresis relation and the loading-unloading stiffness of the specimens. As illustrated in Fig. 10, the theoretical curves of the specimens agreed well with the test results.

Owing to the limitations of the experimental conditions, the quantity and level of the studied parameters were limited, and the dimensions of the specimens were scaled down compared with the columns in the actual project. In future studies, refined models of full-scale STCRSSSC columns can be built using finite elements to analyze the performance of STCRSSSC columns under more key parameters and complex loads to adapt to actual engineering situations.

Based on the experimental study of specimens with specific stress states and geometric characteristics, a prediction model is generally proposed, which has certain limitations in its applicability. However, owing to the randomness and uncertainty of the seismic action, high discreteness of the crack development and bond-slip of concrete, and the fact that the errors of the prediction model are not very sensitive to the results of certain structures, the calculation of the hysteretic behavior of STCRSSSC columns based on the simplified model can still achieve satisfactory results.

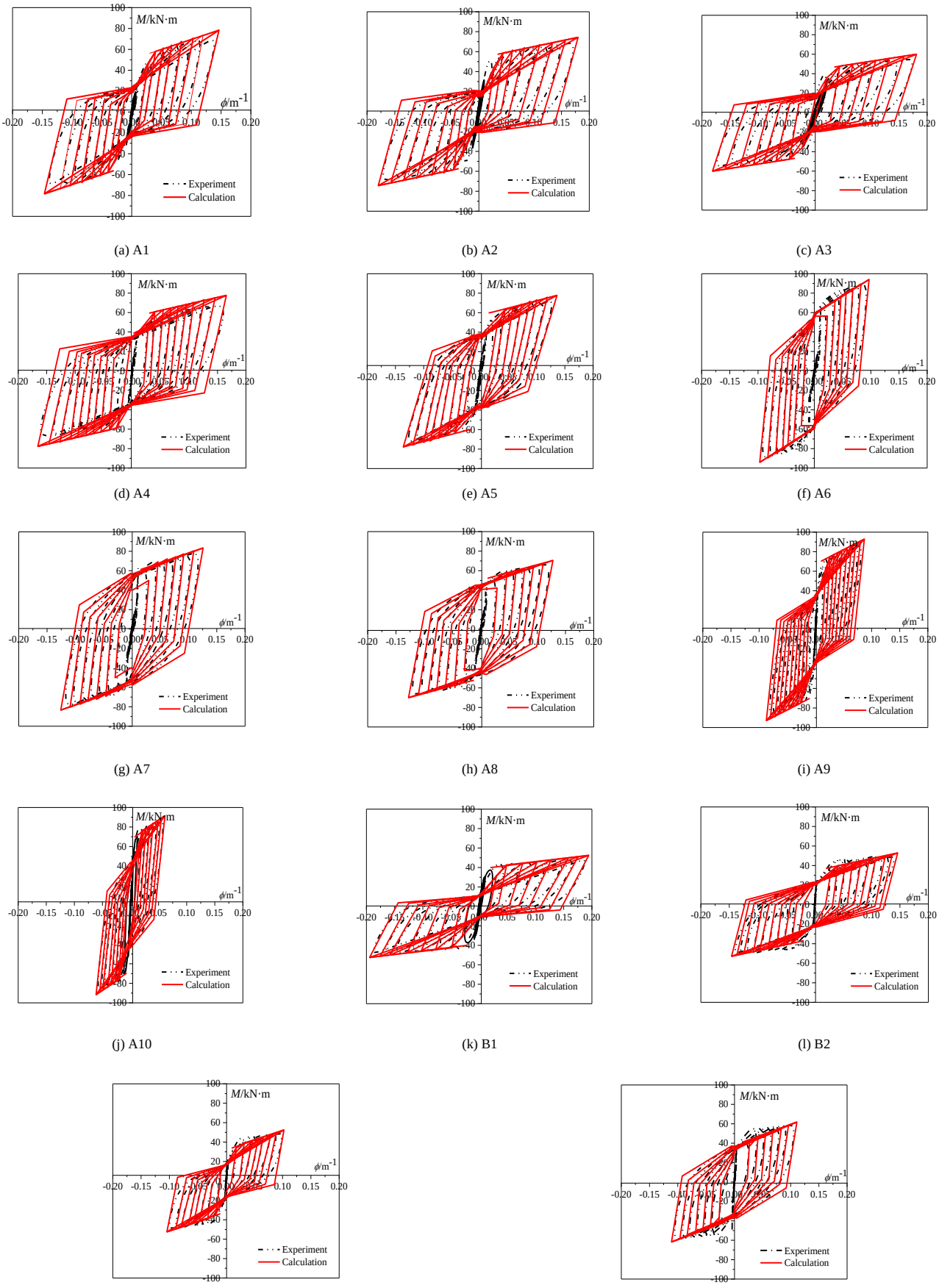

(a) A1 (b) A2 (c) A3

(d) A4 (e) A5 (f) A6

(g) A7 (h) A8 (i) A9

(j) A10 (k) B1 (l) B2

(m) B3 (n) B4

Fig. 10 Comparisons between the theoretical and experimental moment-curvature hysteresis curves

5. Conclusions

This study presents the design and tests of ten STCRSSSC columns and four STCRSSC columns under cyclic loading, investigating the effects of various parameters on seismic performance, including λ, P_{ct}, D/t, and n_0. The conclusions are as follows:

(1) Bending failure occurred in all the specimens, characterized by longitudinal steel bar yield. Circumferential cracks were observed in the non-shear surface at the column bottom, and the core SSSC or SSC was broken at the column bottom. Plastic deformation of the specimens before damage to the STCRSSSC column was significant, with evident signs of failure.

(2) The specimens exhibited plump hysteresis loops with slight pinching. With an increase in D/t or n_0, the plumpness of the hysteresis curves and the areas of the hysteretic loops decreased. However, an increase in λ or P_{ct} increased the area of the hysteretic loops of the hysteresis curves.

(3) The $M-\phi$ skeleton curves are roughly divided into three phases: elastic response, yielding, and failure. With increases in D/t, n_0, and P_{ct}, the slopes of the $M-\phi$ skeleton curves increased. The $M-\phi$ skeleton curves are not significantly affected by λ.

(4) Based on the principle of limiting equilibrium, theoretical calculations of the corresponding yield and ultimate points of the STCRSSSC column were performed based on the experimental studies, and the key characteristic points were connected to a simplified skeleton curve. A comparison of the experimental skeleton curves with the theoretical curves indicated that the model was highly accurate.

(5) Based on the Clough trilinear degeneration model, the hysteresis rule of the $M-\phi$ relationship of STCRSSSC columns is proposed. Furthermore, a prediction model for the performance of the STCRSSSC columns was established and validated.

(6) The proposed prediction model was applied to the STCRSSSC columns. Owing to the limitations of the experimental device, the designed specimen was a third of the actual specimen. Finite element analysis software was used to further analyze the influence of key factors on the behaviors of full-scale specimens in a subsequent study.

Acknowledgments

This study was sponsored by National Natural Science Foundation of China (No. 52078001), Outstanding Youth Fund of Anhui Province (No. 2008085J29), Key Research and Development Project of Anhui Province (No. 2022i01020005), Major Science and Technology Project of Anhui Province (No. 202203a07020005), The University Synergy Innovation Program of Anhui Province (No. GXXT-2023-061, GXXT-2022-074), Wuhu Technology and Innovation Research Institute, Anhui University of Technology (No. 2022jc04), The University Outstanding Research and Innovation Team Program of Anhui Province (No. 2023AH010017).

References

[1] Chin CL, Ma CK, Tan JY, Ong CB, Awang AZ, Omar W. Review on development of external steel-confined concrete. Construction and Building Materials 2019; 211: 919-931. http://doi.org/10.1016/j.conbuildmat.2019.03.295.

[2] Guo L, Liu Y, Fu F, Huang H. Behavior of axially loaded circular stainless steel tube confined concrete stub columns. Thin-Walled Structures 2019; 139: 66–76. https://doi.org/10.1016/j.tws.2019.02.014.

[3] Li WT, Zha XX, Wang HY. A unified formulation for axial compression of steel tube-confined concrete and concrete-filled steel tube stub columns. Structures 2023; 58: 105319. https://doi.org/10.1016/j.istruc.2023.105319.

[4] Zhang J, Ma L, Zhou C, Lee D, Filippou FC. Experimental study of axial compression behavior of circular concrete-filled steel tubes after being loaded at an early age. Construction and Building Materials 2021; 300: 124030. https://doi.org/10.1016/j.conbuildmat.2021.124020.

[5] Zhou XH, Gan D, Liu JP, Chen YF. Composite effect of stub sdquare steel tubed columns under axial compression. Advanced Steel Construction 2018; 14 (2): 274-290. https://doi.org/10.18057/IJASC.2018.14.2.8.

[6] Wang FC, Xie WQ, Li B, Han LH. Experimental study and design of bond behavior in concrete-filled steel tubes (CFST). Engineering Structures 2022; 268: 114750. https://doi.org/10.1016/j.engstruct.2022.114750.

[7] Fu ZQ, Ge HB, Ji BH, Chen JJ. Interface bond behaviour between circular steel tube and lightweight aggregate concrete. Advanced Steel Construction 2018; 14 (3): 424-437. https://doi.org/10.18057/IJASC.2018.14.3.7.

[8] Wang BX, Man T, Jin HN. Prediction of expansion behavior of self-stressing concrete by artificial neural networks and fuzzy inference systems. Construction and Building Materials 2015; 84: 184-191. https://dx.doi.org/10.1016/j.conbuildmat.2015.03.059.

[9] Carballosa P, Calvo JL, Revuelta D., Sánchez JJ, Gutiérrez JP. Influence of cement and expansive additive types in the performance of self-stressing and self-compacting concretes for structural elements. Construction and Building Materials 2015; 93: 223-229. https://dx.doi.org/10.1016/j.conbuildmat.2015.05.113.

[10] Li H, Wang Y, Wang YJ, Liu JP, Tian Q. Effect of CaO and MgO based expansive agent on deformation and mechanical properties of concrete-filled steel tubes. Construction and Building Materials 2020; 250: 118723. https://doi.org/10.1016/j.conbuildmat.2020.118723.

[11] Chang X, Lin HX, Huang CK. Experimental study on shear resistance of self-stressing concrete filled circular steel tubes. Journal of Constructional Steel Research 2009; 65 (4): 801-807. https://doi.org/10.1016/j.jcsr.2008.12.004.

[12] Natalli JF, Andrade HD, Carvalho JMF, Defóveri K, Mendes JC, Sarmanho AMC, et al. Performance of lightweight concrete with expansive and air-entraining admixtures in CFST columns. Journal of Materials in Civil Engineering 2020; 32 (6): 04020121. https://doi.org/10.1061/(ASCE)MT.1943-5533.0003143.

[13] Li X, Pan JL, Xiao Y. Mechanical performance of self-stressing CFST columns under uniaxial compression. Journal of Building Engineering 2021; 44: 103366. https://doi.org/10.1016/j.jobe.2021.103366.

[14] Guo YL, Geng Y, Qu LY. Time-dependent behaviour of circular steel tube confined reinforced concrete (STCRC) stub columns subjected to low axial load. Engineering Structures 2021; 243: 112663. https://doi.org/10.1016/j.engstruct.2021.112663.

[15] Liu ZZ, Huang DM, Li N, Lu YY. Mechanical behavior of steel-fiber-reinforced self-stressing concrete filled steel tube columns subjected to eccentric loading. Structures 2022; 45: 932-950. https://doi.org/10.1016/j.istruc.2022.08.118.

[16] Lu Y, Liu Z, Li S, Li W. Behavior of steel fibers reinforced self-stressing and self-compacting concrete-filled steel tube subjected to bending. Construction and Building Materials 2017; 156: 639-651. https://doi.org/10.1016/j.conbuildmat.2017.09.019.

[17] Yu F, Qin Y, Yao C. Experimental investigation on the seismic behavior of self-stressing steel slag CFST column. Structural Concrete 2022; 23: 1492-1507. https://doi.org/10.1002/suco.202100523.

[18] Lai MH, Zou JJ, Yao BY, Ho JCM, Zhuang X, Wang Q. Improving mechanical behavior and microstructure of concrete by using BOF steel slag aggregate. Construction and Building Materials 2021; 277: 122269. https://doi.org/10.1016/j.conbuildmat.2021.122269.

[19] Nemade PA, Pasla D, Chandrappa AK. Durability assessment of concrete with natural and Linz Donawitz slag as coarse aggregates. Construction and Building Materials 2023; 400: 132617. https://doi.org/10.1016/j.conbuildmat.2023.132617.

[20] Saxena S, Tembhurkar AR. Impact of use of steel slag as coarse aggregate and wastewater on fresh and hardened properties of concrete. Construction and Building Materials 2018; 165: 126-137. https://doi.org/10.1016/j.conbuildmat.2018.01.030.

[21] Ho JCM, Liang Y, Wang YH, Lai MH, Huang ZC, Yang D, Zhang QL. Residual properties of steel slag coarse aggregate concrete after exposure to elevated temperatures. Construction and Building Materials 2022; 316: 125751. https://doi.org/10.1016/j.conbuildmat.2021.125751.

[22] Lai MH, Chen ZH, Wang YH, Ho JCM. Effect of fillers on the mechanical properties and durability of steel slag concrete. Construction and Building Materials 2022; 335: 127495. https://doi.org/10.1016/j.conbuildmat.2022.127495.

[23] Guo YC, Xie JH, Zheng WY, Li JL. Effects of steel slag as fine aggregate on static and impact behaviours of concrete. Construction and Building Materials 2018; 192: 194-201. https://doi.org/10.1016/j.conbuildmat.2018.10.129.

[24] Huang ZC, Ho JCM, Cui J, Ren FM, Cheng X, Lai MH. Improving the post-fire behaviour of steel slag coarse aggregate concrete by adding GGBFS. Journal of Building Engineering 2023; 76: 107283. https://doi.org/10.1016/j.jobe.2023.107283.

[25] Yu F, Fang Y, Niu K, Zhang Y, Chen TY. Experimental study on bond-slip constitutive relation of SSSCFST columns. Structural Concrete 2021; 22(4): 1905-2497. https://doi.org/10.1002/suco.201900546.

[26] Yu F, Cao Y, Fang Y, Zhang Y, Niu K. Mechanical behavior of self-stressing steel slag aggregate concrete filled steel tubular short columns with different loading modes. Structures 2020; 26: 947-957. https://doi.org/10.1016/j.istruc.2020.05.015.

[27] Yu F, Yao C, Hu Y, Fang Y, Niu K, Xiang GS. Axial compressive behavior of self-stressing steel slag aggregate concrete filled steel tubular columns with bond-slip damage. Advanced Steel Construction 2020; 16(1): 13-19. https://doi.org/10.18057/IJASC.2020.16.1.2.

[28] Yu F, Chen T, Niu K, Wang S, Fang Y. Study on bond-slip behaviors of self-stressing steel slag concrete-filled steel tube. KSCE Journal of Civil Engineering 2020; 24: 3309-3319. https://doi.org/10.1007/S12205-020-1596-7.

[29] Wang XL. Study on basic properties of steel slag concrete based on controllable expansion rate. Anhui University of Technology, China. (in Chinese).

[30] GB/T 50081-2002, Standard for test method of mechanical properties on ordinary concrete, Beijing, 2003, China. (in Chinese).

[31] GB/T 50082-2009, Standard for test methods of long-term performance and durability of ordinary concrete, Beijing, 2009, China. (in Chinese).

[32] GB/T 228.1-2010, Metallic materials-Tensile testing-Part 1:Method of test at room temperature, Beijing, 2010, China. (in Chinese).

[33] GB/T 228-2002, Metallic materials-Tensile testing at ambient temperature, Beijing, 2002, China. (in Chinese).

[34] Shang ZQ, Huang CK, Chang X, Xu ST. Experrimental research on shear-resistance properties of self-stressing concrete filled steel tube. Journal of Earthquake Engineering and Engineering Vibration. 2008; 28 (3): 77-81. (in Chinese). https://doi.org/10.13197/j.eeev.2008.03.026.

[35] Gong TN, Xu DF. Seismic performance of reinforced self-compacting concrete-filled circular steel-tube columns. Journal of Constructional Steel Research 2014; 212: 108300. https://doi.org/10.1016/j.jcsr.2023.108300.

[36] Yu F, Xu GS, Niu DT, Cheng AC, Wu P, Kong ZY. Experimental study on PVC-CFRP confined concrete columns under low cyclic loading. Construction and Building Materials 2018; 177: 287-302. https://doi.org/10.1016/j.conbuildmat.2018.05.111.

[37] Chen HY, Liao FY, Yang YX, Ren Y. Behavior of ultra-high-performance concrete (UHPC) encased concrete-filled steel tubular (CFST) stub columns under axial compression. Journal of Constructional Steel Research 2023; 202: 107795. https://doi.org/10.1016/j.jcsr.2023.107795.

[38] Dai S, Zhu HJ, Zhang DR, Liu ZQ, Cheng SY, Zhao JX. Insights to compressive strength, impermeability and microstructure of micro-expansion steel slag cement under constraint conditions. Construction and Building Materials 2022; 326: 126540. https://doi.org/10.1016/j.conbuildmat.2022.126540.

[39] Feng P, Li ZY, Zhang SB, Yang JQ. Steel slag aggregate concrete filled-in FRP tubes: Volume expansion effect and axial compressive behaviour. Construction and Building Materials 2022; 318: 125961. https://doi.org/10.1016/j.conbuildmat.2021.125961.

[40] Chen TY. Experimental study and theoretical analysis on seismic behavior of circular tube confined reinforced self-stressing of steel slag concrete columns, Anhui University of Technology, China. (in Chinese).